

Fly, Track, Land: Infrastructure-less Magnetic Localization for Heterogeneous UAV–UGV Teaming

Valerio Brunacci, Davide Plozza, Alessio De Angelis, Michele Magno, *Fellow, IEEE*, Tommaso Polonelli, *Senior Member, IEEE*

Abstract—

We present a complete infrastructure-less magneto-inductive (MI) localization system enabling a lightweight UAV to autonomously hover, track, and land with centimeter precision on a mobile quadruped robot acting as a dynamic docking pad. This work advances the vision of heterogeneous robot collaboration, where ultra-lightweight flying robots serve as mobile perception agents for ground-based Unmanned Ground Vehicles (UGVs). By extending the sensing horizon and providing complementary viewpoints, the UAVs enhance exploration efficiency and improve the quality of data collection in large-scale, unknown environments. The proposed system aims to complement traditional localization modalities with a compact, embedded, and infrastructure-less magnetic sensing approach, providing accurate short-range relative positioning to bridge the gap between coarse navigation and precise UAV docking. A single lightweight receive coil and a fully embedded estimation pipeline on the UAV deliver 20 Hz relative pose estimates in the UGV’s frame, achieving a 3D position root-mean-square error (RMSE) of 5 cm. The system uses real-time estimation and a warm-started solver to estimate the 3D position, which is then fused with inertial and optical-flow measurements in the onboard extended Kalman filter. Real-world experiments validate the effectiveness of the framework, demonstrating significant improvements in UAV–UGV teaming in infrastructure-less scenarios compared to state-of-the-art methods, requiring no external anchors or global positioning. In dynamic scenarios, the UAV tracks and docks with a moving UGV while maintaining a 7.2 cm RMSE and achieving successful autonomous landings.

I. INTRODUCTION

With the increasing popularity of multi-robot swarms, collaborative exploration and mission planning have gained significant scientific attention [1], [2]. However, current research predominantly focuses on homogeneous robot teams [3], [4], leaving substantial opportunities for advancing collaboration between ground and aerial platforms [5]. Recently, heterogeneous robotic teams have attracted growing interest for applications where complementary capabilities can be effectively leveraged [6], [7]. In particular, unmanned aerial vehicles (UAVs) [8] have emerged as agile and easily deployable aerial perception agents that can complement unmanned ground vehicle (UGVs) such as quadrupeds or wheeled robots [9]. For instance, nano-scale palm-sized UAVs can access elevated

vantage points or confined spaces beyond the reach of ground robots, while larger UGVs can transport heavier payloads and host more powerful sensing and computing resources for mapping and navigation [10]. This synergy combines the mobility and rapid scouting capability of aerial robots with the endurance and sensing capacity of ground platforms [6]. Leveraging the complementary characteristics of heterogeneous robotic swarms can substantially enhance exploration performance and mission efficiency. In such systems, UGVs provide payload capacity and long operational endurance, while aerial robots contribute agility and maneuverability. For example, a nano-UAV deployed from a legged robot can scout difficult-to-access areas [11] and subsequently return to the UGV for data transfer or battery recharging, enabling more informed and globally consistent task planning.

Such marsupial robot configurations have been proposed to maximize mission coverage and efficiency [6]. Indeed, recent efforts integrated a micro-drone with a quadruped as a mobile launch/landing pad [6], and NASA’s *Ingenuity* Mars helicopter (a 1.8 kg UAV) demonstrated the benefits of aerial–ground cooperation by scouting ahead of the *Perseverance* rover [12]. These examples motivate our focus on enabling a nano-UAV to precisely land on a mobile UGV – a capability that can significantly enhance the deployability of future robot teams in the field [8], [13].

A fundamental challenge to enable heterogeneous robotic collaborations relies in achieving robust relative localization between the nano-UAV and the moving UGV with the accuracy needed for docking [8]. Conventional solutions such as UWB ranging and GNSS (including RTK variants) are widely used to provide global or relative positioning over meter-scale workspaces [14]–[16]. Moreover, GNSS can be unavailable or unreliable indoors, in urban canyons, underground, or in planetary-like scenarios, motivating infrastructure-less relative sensing for close-proximity interaction [17]. In practice, their achievable accuracy strongly depends on deployment and operating conditions (e.g., anchor geometry and calibration for UWB, or correction availability for GNSS), and their role is often best suited to coarse acquisition, navigation, and rendezvous at longer ranges. However, during the *final docking phase* onto a compact, mobile interface (tens of centimeters), even residual decimeter-level relative errors can lead to missed contact or unsafe interactions, motivating sensing modalities that are specifically effective at close range [11].

Vision-based relative localization can provide high precision by detecting fiducial markers or recognizable features on the UGV [18]–[20]. However, vision performance depends

This work has been supported by the European Commission HORIZON project RADIANCE, ID: 101235536 DOI: <https://doi.org/10.3030/101235536>. V. Brunacci is with the Department of Engineering, University of Perugia, 06125 Perugia, Italy, and also with the Multi-Robot Systems Group, Faculty of Electrical Engineering, Czech Technical University in Prague, 16627 Prague, Czech Republic. A. De Angelis is with the Department of Engineering, University of Perugia, 06125 Perugia, Italy. T. Polonelli, D. Plozza, and M. Magno are with the D-ITET Department, ETH Zürich, 8092 Zürich, Switzerland.

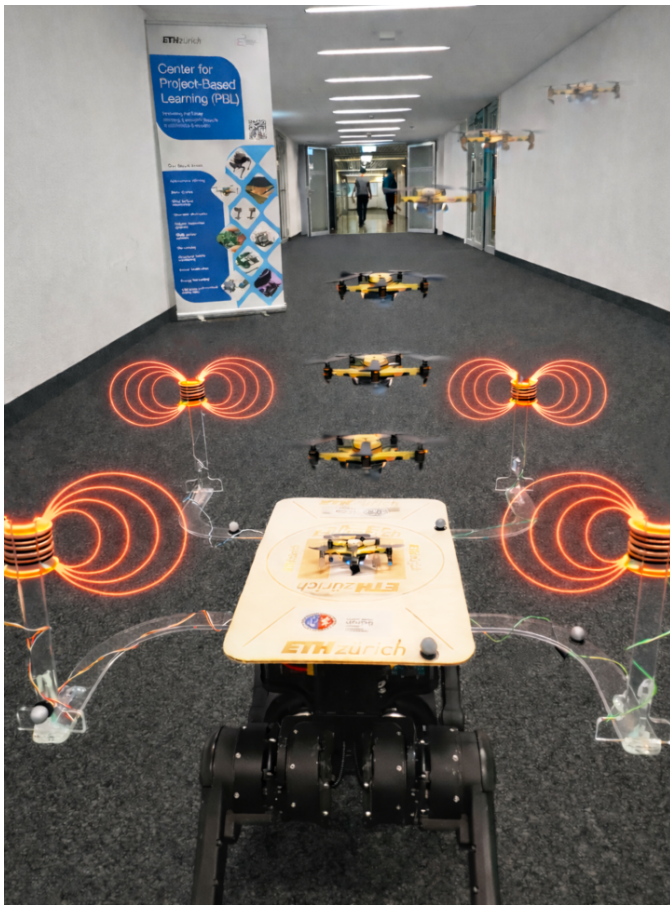


Fig. 1: Representative picture of a nano-size UAV autonomously landing on a moving legged robot and GNSS-denied environment. The infrastructure-free localization system relies on onboard sensors, combining IMUs, optical-flow camera, UWB, and the MI system. The four reference coils are represented by the red lines with a magnetic dipole shape. The landing deck can be used to recharge the UAV's batteries.

on favorable illumination and unobstructed line-of-sight, and can degrade in darkness, dust, smoke, or cluttered scenes – conditions frequently encountered in realistic deployments [6]. Moreover, ultra-lightweight nano-UAVs face strict SWaP limits, which restrict camera choice, onboard compute, and the complexity of perception pipelines [8]. In summary, existing modalities offer strong advantages at different scales, but none alone consistently satisfies the combined requirements of *infrastructure-less*, close-range, centimeter-accurate docking onto a moving UGV in challenging environments.

To bridge this gap, we propose a magneto-inductive (MI) relative localization approach tailored for the final stage of UAV–UGV docking. Magnetic field-based localization offers several attractive properties for a close-range positioning system. Magnetic fields (in the ~ 200 kHz range) do not require direct line-of-sight, and their spatial decay provides a natural signal gradient for positioning. By equipping the UGV with a small oscillating magnetic field emitters (coils) and the nano-UAV with lightweight magnetometer custom sensor, we create a local magnetic “beacon” that the UAV can sense and navigate toward. The effective range of MI localization is inherently

limited – typically a tens of centimeters at most, since field strength falls off rapidly (with roughly $1/r^3$ for a dipole source) [21]. However, MI localization can achieve very fine-grained positioning, in the range of ~ 1.5 cm [22].

Prior researches have hinted the potential of MI localization: for example, the work [21] showed that a UAV can track its position relative to a current-carrying wire (power line) using the induced magnetic field, even while moving at 8 m s^{-1} and up to 4 m away. Similarly, in [23], authors used an inductive coil system to localize a UAV for wireless charging alignment, consistently achieving ~ 20 cm accuracy in flight tests. These works, though focused on specific scenarios (perching on wires or hovering over a charging pad), demonstrate that magnetic sensing can be leveraged for precise relative positioning in GNSS- or vision-denied environments. Unlike previous methods, we exploit the magnetic principle for UAV-on-UGV tracking and landing: the MI sensor system is engaged during the final approach, where it can guide the nano-UAV into a docking position with the necessary accuracy. Notably, this MI-based localization is naturally complementary to UWB/GNSS ranging [8], [14] – common localization systems can handle long-range acquisition and homing until the UAV is close to the UGV, at which point the magnetic system takes over to refine the relative pose for a smooth, precision touchdown. This two-tiered strategy combines the strengths of each technology in a single multi-modal infrastructureless relative localization system. This capability has immediate practical benefits (e.g., autonomous battery charging between a drone and its mobile ground base in the field), and also serves as a stepping stone toward more advanced heterogeneous robot teams [5]. Looking forward, the integration of flying micro-robots with mobile ground robots is an important paradigm for future robot swarms and exploratory missions [24]. Precise relative navigation and docking allow such teams to share resources, extend operational range, and autonomously re-configure. Additionally, such configurations naturally allow aerial robots to provide complementary viewpoints for environment perception in the immediate surroundings of the ground platform [25], [26]. This aspect is particularly relevant given that recent state-of-the-art perceptive locomotion and navigation approaches for quadrupedal robots emphasize onboard, robot-centric perception strategies that inherently restrict environmental awareness to the robot's immediate surroundings [27], [28]. This limitation is further exacerbated in compact quadrupedal systems, where limited space and physical integration constraints restrict the sensing configurations that can be deployed onboard [29].

Motivated by these considerations, this work introduces an heterogeneous air-ground robotic system based on an infrastructureless MI anchor-tag localization, including a real-world implementation and evaluation on a quadruped UGV and a nano-UAV. Four frequency-multiplexed transmit coils mounted on the UGV provide a mobile magnetic reference, while a lightweight 9 g receiving coil and embedded estimator on the UAV deliver 20 Hz relative pose updates fused directly into the UAV flight controller. The entire stack respects the mass, power, and compute constraints of the nano-UAV, enabling hovering, relative tracking, and precision landing on a moving

docking pad without *external* cameras, fiducials, or GNSS.

The proposed system is designed as an onboard multimodal localization architecture: the MI module provides short-range relative position updates directly fused into the nano-UAV state estimator, while the same EKF interface natively supports UWB for longer-range acquisition and homing—making hierarchical integration straightforward without additional software effort. In this paper, we deliberately isolate the MI contribution: UWB-based relative localization is already extensively characterized in the literature [14], [15] and its typical accuracy (10–30 cm) is better suited to long-range acquisition and homing than to the centimeter-accurate final docking phase, which is the focus of this work.

We validate the approach in extensive experiments instrumented with a motion capture system (used only as ground truth). Hovering and landing over a stationary base achieve centimeter-level 3D RMSE and tight touchdown dispersion, with a success rate of 100%, while tracking and docking on a moving UGV maintain approximately 8 cm to 11 cm RMSE.

In summary, this paper makes the following technical contributions: (i) The design of an infrastructure-less localization framework for heterogeneous UAV–UGV teams based on MI, with hierarchical fusion alongside conventional global and local positioning modalities such as UWB and GNSS. Unlike passive or quasi-static magnetic docking aids, the proposed active AC frequency-multiplexed MI system targets the final close-range docking phase (within 1 m), enabling a structured measurement model for unambiguous 3D relative position estimation while naturally complementing coarser modalities that handle long-range acquisition and homing. (ii) A fully onboard real-time estimation pipeline that models the magnetic dipole fields directly on the nano-UAV microcontroller at 20 Hz, delivering relative position updates fused into the UAV state estimator within the strict SWaP constraints of nano-scale platforms. (iii) Extensive real world validation on a nano-UAV and a quadrupedal UGV, demonstrating centimeter level precision landing on a stationary platform and sub decimeter dynamic tracking on a moving ground robot, without external infrastructure, fiducials, or GNSS.

II. RELATED WORK

Combining aerial and ground robots into cooperative teams has gained significant attention for missions that demand both endurance and mobility [24], such as planetary exploration [12], subterranean mapping [6], search and rescue [10], and infrastructure inspection [30]. Ground robots—particularly legged platforms like quadrupeds—offer payload capacity, energy efficiency, and stable locomotion across uneven terrain [31]. However, their sensing capabilities are limited by their low vantage point and occlusions near ground level [27], [28]. This restricts their ability to perceive upcoming terrain features, particularly negative obstacles such as drop-offs or gaps, or to navigate around obstacles beyond their immediate field of view. Prior works have therefore explored the use of aerial companions to compensate for these limitations, enabling real-time overhead imagery [24], traversability assessment, or 3D mapping from dynamically changing viewpoints [12], [19].

Such a configuration enables truly collaborative autonomy, where the UAV enhances the perception and planning of the UGV, and the UGV in turn provides computational support, energy, or physical transport for the UAV [19]. Numerous works have demonstrated UAV–UGV teams in exploration, mapping, and target tracking [32]. A common framework is a UGV serving as a mobile base or “hub” for UAVs [33]. For example, in search & rescue scenarios, a UGV can carry extra batteries or sensors, and a UAV deploys from it to survey areas and then returns to the UGV for data transfer or charging [34]. This requires the UAV to localize relative to the UGV *without* relying on external infrastructure. Space robotics offers a compelling real-world precedent [12]: NASA’s Perseverance rover and its aerial companion, the *Ingenuity* helicopter, demonstrated that heterogeneous robot teams can outperform monolithic systems by combining sensing perspectives and operational ranges [12]. Inspired by this paradigm, recent terrestrial efforts have explored tightly coupled UAV–UGV systems for deployment in GNSS-denied and infrastructure-free environments [17], [35].

However, these missions face multiple challenges. GNSS and GPS-based localization, while widely used, are often unavailable or unreliable in cluttered urban canyons, indoors, underground, or on other planets [17]. Even when GNSS is available, its typical accuracy (on the order of 1 m to 3 m) is inadequate for high-precision coordination or docking maneuvers [16]. To overcome these challenges, a wide range of approaches have been proposed for relative localization and docking in air–ground systems, which we explore in detail in the following subsections and compare with our work in Table I.

A. Relative Localization for Teaming Heterogeneous Robots and Docking

A wide body of work explores relative localization to support collaboration [7], [8], [14]. Vision-based methods are among the most accurate [36]: fiducial markers (e.g., AprilTags [37]) or model-based object detection can yield centimeter-scale pose estimates under ideal conditions. However, their dependence on line-of-sight, good illumination, and high camera frame rates makes them unreliable in cluttered or fast-changing environments [38]. Moreover, the ultra-lightweight UAVs suitable for scouting from a legged robot—such as Crazyflie-class nano-drones—face extreme constraints in computation, payload, and sensor quality, which limit their ability to run conventional perception pipelines [8], [14]. Onboard cameras with wide-angle lenses or dedicated neural detectors partially address this [20], but often exceed the SWaP (size, weight, and power) capabilities of nano-UAVs [8].

Radio-frequency methods, especially UWB [15], offer robustness to lighting and occlusion and have been used in both fixed-anchor and peer-to-peer setups [8], [14]. UWB allows fully mobile teams to localize one another without infrastructure [14], but the achievable accuracy (typically 10 cm to 30 cm) falls short for tasks requiring precise relative pose for landing and docking [39]. This limitation is visible even on Crazyflie-scale persistent autonomy: Nguyen *et al.* [40]

rely on an anchor-based loco positioning system for tracking, but switch to a multi-ranger (laser ToF) deck during the landing phase to reduce horizontal error and achieve reliable pad contact. Moreover, multiple antennas or cooperative estimation algorithms are often needed to infer full 6-DOF pose [14], adding system complexity and calibration burden. Some systems employ an “on-body anchor” strategy, where the UGV aids localization by carrying markers and beacons [17]. In [41], for example, a UGV emits visual or UWB signals for UAV tracking and homing. Cooperative localization filters have also been proposed, combining the UGV’s odometry with the UAV’s observations to maintain a shared relative estimate [17]. These approaches remove the need for fixed infrastructure, but still face accuracy and robustness trade-offs in dynamic or cluttered scenes.

Current trends point toward sensor fusion: combining modalities like vision, RF ranging, and inertial data to maximize robustness across environments [17], [42]. Recent reviews [42] converge on a key insight: no single sensing modality suffices for robust air-ground coordination across all conditions. Instead, fusing complementary sensors—each optimized for different stages or scales of the task—is the emerging trend [43]. However, integrating such systems on small-scale UAVs remains a challenge due to tight SWaP constraints [8].

As robotic collaboration expands toward larger, autonomous teams—such as drone-quadruped formations in underground or extraterrestrial missions—there is growing demand for centimeter-precision, infrastructure-free localization methods that are resilient, low-power, and compatible with ultra-light aerial platforms [8]. As visible from Table I, this paper is bridging this gap enabling close aerial-ground cooperation by introducing MI localization as a complementary sensing modality for close-proximity UAV-UGV teaming, particularly suited to the final stages of coordinated tasks such as landing, battery charging, mapping, tracking, or deployment. Compared with previous methods listed in Table I, our work sidesteps the limitations of common localization approaches, e.g., GNSS, camera-based, and UWB range resolution, while being lightweight enough for integration into centimeter-scale UAVs. It supports a new class of tightly integrated, heterogeneous robotic teams suitable for autonomous deployment in unstructured and GNSS-denied environments.

A particularly challenging case of UAV-UGV cooperation is autonomous landing of a UAV on a *moving* UGV. This is essentially a precision pursuit-evasion problem: the UAV must not only track the UGV’s pose but also descend and land, often within a limited “landing zone” area on the UGV. A critical requirement here is robust disturbance rejection and trajectory planning, where the UAV needs to anticipate the UGV’s motion. Many solutions maintain a constant offset or approach from behind to account for UGV forward motion [44]. Approaches like Baca [45] used a fisheye camera for a wide view of the moving target and a Kalman filter to estimate its trajectory, then guided the UAV in for landing. Mobile docking requires careful software solutions: the literature emphasizes robustness for uncertainty aware path planners (ability to land despite disturbances or sudden UGV maneuvers) as a

primary metric for success [46]. The state of the art now includes demonstrations of UAVs landing on UGVs that are not only moving but possibly adapting – e.g., a UGV with a self-leveling platform to assist the UAV [47]. Still, there are open research gaps: multi-UAV, single-UGV coordination (scheduling which drone lands when, to avoid conflicts) and performing this reliably without GNSS or motion capture [17], [48]. A body of work focuses on persistent docking of UAVs for battery recharge or payload transfer [48]. These systems often employ custom fiducials for final alignment [49]. For instance, a number of recent designs use wireless charging pads that guide the UAV visual markers into a receptacle for inductive charging [50]. The systems in [50], [51] combines downward camera-based marker detection with precision flight control to land on a charging pad, achieving reliable contact for recharging [48]. The emphasis in such works is on ensuring physical alignment (to connect power terminals or coils) with a sub centimeter-level precision, needed for accurate landing and inductive battery recharging on a moving target [48]. IR-LOCK [52] is one commercial example, using an IR beacon on the pad and a filtered IR camera on the drone to zero in on the hotspot – effective indoors, but essentially a homing sensor rather than a general localization solution. Mechanical docking stations with funnels or self-aligning mechanisms have also been developed, reducing the required landing precision at the cost of added weight on the docking platform [53]. These solutions highlight practical infrastructure for autonomy, but they typically assume a mostly static or pre-known landing site. Unlike our scenario of mobile landing on a UGV, standard docking pads do not estimate the relative 3D pose during approach – they often presuppose the UAV navigates itself near the pad using other means, then use short-range guidance (vision or IR) for the final meter. Some docking systems also exploit permanent magnets or electromagnets to provide short-range attraction and self-alignment (e.g., [39]); however, these approaches function as passive alignment aids rather than structured sensing systems, providing short-range attraction but no measurement model for 3D pose estimation, a fundamental distinction from the active AC MI system proposed in this work. In summary, vision-based landing offers high precision but can be fragile to lighting and line of sight [38] and require heavy processing; range and RF methods are more tolerant to environment but provide less precision without infrastructure. None of these categories simultaneously satisfy the centimeter-scale accuracy, infrastructure independence, and strict payload/power envelope demanded by nano-UAV platforms teamed with moving UGVs, motivating the magneto-inductive localization alternative explored in this work.

B. Magneto-Inductive and Near-Field Magnetic Localization

MI localization leverages low-frequency magnetic fields that decay with $1/r^3$, making them inherently robust to multipath effects and largely unaffected by non-ferromagnetic occlusions [54], [55]. Most systems model the transmitters as magnetic dipoles—small coils generating predictable axial and transverse field patterns in free space [56]. This dipole

approximation is accurate when the receiver is located several coil diameters away but becomes less reliable at close ranges. For applications such as drone docking at ~ 0.5 m with coil diameters of 5 cm to 10 cm, the system operates near the limits of dipole model validity [57]. Mutual inductance models or geometric corrections may be necessary to achieve sub-centimeter accuracy in fields spanning ~ 30 cm.

3D localization requires distinguishing fields from multiple transmitters. We adopt frequency-division multiplexing (FDM), in which each coil broadcasts a sinusoidal signal at a distinct frequency. The UAV onboard magnetometer (see Figure 2) measures the superimposed field, and spectral decomposition (e.g., FFT) isolates individual coil contributions [56]. FDM enables continuous sampling but requires careful frequency spacing to avoid mixing artifacts [58]. Coil LC resonance is tuned to maximize field strength (high Q factor), and signal amplitudes are calibrated to avoid saturating the receiver’s ADC, especially at close proximity. Position estimation relies on solving an inverse magnetic problem: given known coil positions and field vectors at the receiver, compute the 3D receiver position (and potentially orientation). Simpler systems use only range estimation via the $1/r^3$ decay, but this ignores orientation and cross-axis coupling. More general solutions involve nonlinear optimization, such as gradient descent (e.g., Nelder–Mead), Gauss-Newton methods, or global search techniques [59]. Filters like the Unscented Kalman Filter (UKF) have been applied to track coil pose in real-time, enabling sub-centimeter accuracy [57]. Our implementation simplifies the problem by using IMU-based attitude estimation from the Crazyflie, reducing magnetic inversion to position-only estimation.

Notably, MI localization is resilient to lighting conditions and visual occlusion—smoke, walls, or darkness have negligible impact on low-frequency magnetic fields. Unlike RF, MI systems are immune to multipath and reflections from materials like wood or concrete, which have relative permeability close to unity [56]. However, nearby ferromagnetic materials or conductors can introduce bias or attenuation due to eddy currents. We mitigate this with in-situ calibration and analog/digital filtering focused on narrow frequency bands of interest. Motor EMI from the drone is filtered out due to its distinct frequency content [60]. Our system complies with EMC safety standards, as our frequencies (tens of kHz) and field strengths are comparable to wireless charging systems and confined within the near-field region.

MI tracking has proven effective in specialized applications such as biomedical implant localization and AR/VR headsets, achieving millimeter-level accuracy in ~ 30 cm to 50 cm volumes [57]. More recently, MI systems have been deployed in mining and underwater robotics where RF fails [56]. In mobile robotics, however, their use for aerial docking or robot teaming remains limited. Our system demonstrates MI localization as a viable solution for nano-UAV landing in indoor or GNSS-denied settings, offering a precise, infrastructure-free alternative to visual or UWB-based approaches under severe SWaP constraints.

III. MAGNETIC MODEL & ESTIMATOR

We consider a heterogeneous air–ground system composed of a quadruped UGV equipped with $N = 4$ transmitting coils (anchors) and a nano-UAV carrying a single receiving coil (tag). Let $\{\mathcal{B}\}$ denote the inertial frame attached to the UGV (anchor frame), and $\{\mathcal{T}\}$ the body frame rigidly attached to the UAV. The system geometry is defined by the fixed configuration of the anchors on the ground unit. The i -th transmitting coil is located at a known position $\mathbf{p}_i^{\mathcal{B}}$ relative to the UGV center. To simplify the setup, the anchors are mounted with their magnetic axes strictly perpendicular to the UGV horizontal plane; consequently, the orientation vector \mathbf{u}_i of each transmitter is fixed and aligned with the vertical axis of the reference frame (i.e., $\mathbf{u}_i \parallel \mathbf{z}_{\mathcal{B}}$). On the receiving side, the tag coil is rigidly mounted to the UAV airframe. Its orientation is defined by the local unit normal $\mathbf{n}^{\mathcal{T}}$, which is constant in the body frame $\{\mathcal{T}\}$. However, since the coil rotates integrally with the drone, its effective orientation in the anchor frame, denoted as $\mathbf{n}^{\mathcal{B}}$, varies over time. This vector is continuously reconstructed using the UAV’s onboard attitude estimate via the rotation matrix $\mathbf{R}_{\mathcal{T}}^{\mathcal{B}}$ provided by the flight controller (i.e., $\mathbf{n}^{\mathcal{B}} = \mathbf{R}_{\mathcal{T}}^{\mathcal{B}} \mathbf{n}^{\mathcal{T}}$).

The estimation problem consists of determining the unknown position of the tag $\mathbf{x}^{\mathcal{B}} \in \mathbb{R}^3$ expressed in the anchor frame $\{\mathcal{B}\}$, relying on the magnetic interaction between the ground-based sources and the airborne receiver. Selecting an appropriate magnetic-field model is a design choice that balances physical fidelity, computational cost, and the operating envelope of the application. In magnetic positioning (MPS) systems—where small coils generate and sense fields to infer range, bearing, or pose at short to mid distances—the sources are typically compact [57], the environment is weakly dispersive, and the frequencies are chosen to avoid strong radiation while maintaining sufficient signal-to-noise-ratio (SNR). Under these conditions, different modeling layers can be invoked with increasing simplification [57]. In the following, the list of numerical solvers considered for our MPS system. (i) Full Maxwell (complete time-varying EM fields) is the most general framework and captures induction, displacement current, radiation, and material dispersion. It is required when the geometry is not electrically small, when the operating frequency pushes the system toward the radiative regime, or when complex media (lossy, anisotropic, nonlinear) and intricate couplings must be resolved. In practice, one solves the field equations numerically (e.g., FEM/BEM/FDTD) with detailed boundary conditions. This level offers the highest accuracy at the expense of significant modeling effort and computational load [62]. (ii) Magnetoquasistatic / Biot–Savart works well when dimensions are small compared to the electromagnetic wavelength and radiation is negligible, the problem reduces to a near-field, induction-dominated regime. Currents (or current densities) are treated as the primary sources, and the magnetic field is obtained by integrating their contributions over the conductors. This description is well suited to coils and compact windings, provides high accuracy in the near field, and naturally accommodates arbitrary geometries. It remains more demanding than closed-form models but is substantially

TABLE I: Comparison of UAV-UGV landing and cooperative systems in recent literature.

Paper	Localization Method	Infrastructure-less	Moving Landing	Landing metric	UAV-UGV Teaming	Field Test	Nano-UAV
[17]	UWB+IMU+Vision	✗	✓	-	✗	Outdoor	✗
[41]	UWB ranging (2 UAVs)	✓	✗	14 cm	✓	Outdoor	✗
[34]	GNSS + UWB	✗	✗	±10 cm	✗ (static sensors)	Outdoor	✗
[61]	Vision + motion	✓	✓	±5°	✗	Simulation	✗
[20]	Vision	✓	✓	80% SC	✗	Sim. + Indoor	✓
[24]	SLAM (shared map.) + manual	✗	✗	-	✓	Outdoor	✗
[8]	UWB + Vision	✗	-	30 cm	✗	Indoor	✓
[14]	UWB	✓	-	39 cm	✗	Indoor	✓
[7]	restricted	✓	✗	-	✓ (rover)	Moon/Mars	✓
[19]	GNSS + Vision	✗	✓	20 cm to 60 cm	✓	Simulation	✗
[22]	UWB + MI	✗	✗	7 cm	✗	Outdoor	✗
[39]	MI + Vision	✗	✗	~1 cm	✗	Sim. + Indoor	✗
[35]	Vision	✗	✗	-	✓	Indoor	✗
[48]	MI	✓	✗	-	✗	-	✗
[46]	Mechanical	✗	✓	4.5 cm	✓	Indoor	✗
[36]	Vision	✗	✓	±20 cm	✓ (boat)	Outdoor	✓
This work	MI (+UWB)	✓	✓	7.2 cm	✓	✓	✓

lighter than a full electromagnetic simulation. (iii) Magnetic dipole (compact-source approximation) approach can be used if the transmitter coil is physically small compared to the Tx–Rx separation and the region of interest, the entire source can be summarized by its magnetic moment and associated orientation. The resulting field admits a simple closed-form expression with the expected inverse-cube decay and a clear geometric dependence. This approximation is extremely attractive for magnetic positioning: it yields analytic expressions, enables fast evaluation and fitting, and is easy to differentiate for estimation and control, provided the use case respects its validity constraints (compact source, near-field dominance, linear media, modest frequency) [63]. In our scenario, the coil dimensions and operating frequency, together with the Tx–Rx separations of interest, place the system within the compact-source, near-field regime. We therefore adopt the *magnetic dipole* model: it satisfies the applicability constraints of the use case and is the least computationally expensive option, enabling closed-form real-time predictions and efficient inference for magnetic positioning.

A. Measurement Model

We consider a magnetic-positioning setup based on coils acting as source and sensor: a transmitting (TX) coil generates a time-varying magnetic field, and a receiving (RX) coil senses its effect. Operation is in the near field at separations that begin at distances \gg larger than the coil dimensions, so that the source is compact relative to the TX–RX spacing and the environment is well approximated as linear, homogeneous, and isotropic. In this compact-source regime, and provided that the orientations of both TX and RX are known (unit normals $\hat{\mathbf{n}}_t$ and $\hat{\mathbf{n}}_r$), we model the TX coil as a magnetic dipole with moment $\mathbf{m}(t) = N_t I(t) A_t \hat{\mathbf{n}}_t$, where t is time, N_t is the number of turns of the transmitting coil and A_t is its cross-sectional area. The dipole field in closed form at an observation point \mathbf{r} , with $\hat{\mathbf{r}}$ the unit vector from the TX to \mathbf{r} and $r = \|\mathbf{r}\|$, is defined in Equation (1). However, since the system operates under harmonic excitation in the magneto-quasistatic regime, and the positioning algorithm processes signal amplitudes (e.g., via FFT extraction), it is possible to

henceforth suppress the explicit time dependence t . Therefore, the formulations used in the estimation pipeline rely on the phasor magnitudes in Equation (2), where I represents the constant current amplitude (peak or RMS).

$$\mathbf{B}(\mathbf{r}, t) = \frac{\mu_0}{4\pi r^3} [3(\mathbf{m}(t) \cdot \hat{\mathbf{r}}) \hat{\mathbf{r}} - \mathbf{m}(t)] , \quad (1)$$

$$\mathbf{m} = N_t I A_t \hat{\mathbf{n}}_t, \quad \mathbf{B}(\mathbf{r}) = \frac{\mu_0}{4\pi r^3} [3(\mathbf{m} \cdot \hat{\mathbf{r}}) \hat{\mathbf{r}} - \mathbf{m}] , \quad (2)$$

Because we use an identical coil on the RX side as magnetic filed sensor¹, it is possible to relate the coupled magnetic field \mathbf{B} at the receiver via the relative measured voltage to the range r and to the relative orientation.

Since the system operates at a known fixed frequency, the magnitude of the induced electromotive force is directly proportional to the angular frequency ω , the magnetic flux amplitude and the amplifier gain at the RX stage. The measured voltage amplitude V_{rx} in Equation (3) is modeled by explicitly separating the physical induction terms from the electronic amplification, where: (i) G_{RX} represents the total configurable electronic gain of the measurement chain; (ii) $\omega = 2\pi f$ is the angular resonance frequency; (iii) N_r and A_r are the number of turns and the cross-sectional area of the receiving coil, respectively; (iv) $\hat{\mathbf{n}}_r$ is the unit normal vector of the receiving coil. Equation (3) relates the geometric properties of the field (via the dot product $\mathbf{B} \cdot \hat{\mathbf{n}}_r$) to the scalar value processed by the estimation algorithm.

$$V_{rx} = \underbrace{G_{RX}}_{\text{RX Gain}} \cdot \underbrace{(\omega N_r A_r)}_{\text{Transduction Factor}} \cdot \underbrace{|\mathbf{B}(\mathbf{r}) \cdot \hat{\mathbf{n}}_r|}_{\text{Magnetic Flux}} . \quad (3)$$

B. Localization Method

The localization pipeline runs entirely onboard the nano-UAV MCU. It involves three main stages: signal extraction, initial calibration, and iterative position estimation.

¹ There exist sensors that directly report \mathbf{B} (e.g., Hall-effect devices), but commercially available options that operate at the frequencies and with the sensitivity relevant to this work are not easily sourced; hence the coil-based, voltage-sensing approach adopted here.

Signal Extraction and Calibration: The raw signal from the coils is sampled by the ADC and processed via FFT with a flattop window to minimize scalloping loss. The amplitude of the peak corresponding to the i -th anchor, denoted as $\tilde{V}_{raw,i}$, with $i = 1 \dots 4$, is extracted from the FFT and refined using parabolic interpolation. To map the resulting raw digital values to the physical model in Equation (3), a one-time static calibration is performed before flight during system startup (procedure defined in Algorithm 1). During calibration, the UAV is placed at a known reference pose \mathbf{x}_{ref} (the origin of the anchor frame), and the system computes a per-anchor calibration coefficient $C_i = \tilde{V}_{raw,i}(\mathbf{x}_{ref})/V_{model,i}(\mathbf{x}_{ref})$ that lumps the electronic gain G_{RX} and the transduction factors, where $V_{model,i}$ is the theoretical voltage predicted by (3). During operation, the calibrated measured voltage is simply obtained as $V_{meas,i} = \tilde{V}_{raw,i}/C_i$.

Position Estimation via Optimization: The core of the localization module is a numerical optimizer that solves the inverse magnetic problem: finding the position \mathbf{x} that best explains the observed induced voltages at different bandwidths. Unlike trilateration approaches that typically rely on intermediate range estimates, our method directly infers the 3D coordinate \mathbf{x} from the signal amplitudes, thereby preserving the full geometric information contained in the dipole field. We formulate this in Equation (4) as a nonlinear least-squares problem minimizing the residual between the model predictions and the calibrated measurements, where Ω represents the search space (box constraints) corresponding to the valid flight volume.

$$\hat{\mathbf{x}} = \arg \min_{\mathbf{x} \in \Omega} \sum_{i=1}^N (V_{model,i}(\mathbf{x}, \hat{\mathbf{n}}_r) - V_{meas,i})^2. \quad (4)$$

We employ the *Nelder-Mead* simplex algorithm for this minimization. This derivative-free method is well-suited for embedded implementation as it is robust to signal noise and does not require computationally expensive Jacobian calculations. To ensure real-time performance (equivalent to an update rate ≈ 20 Hz), the optimizer utilizes a warm-start strategy: the simplex is initialized around the previous position estimate $\hat{\mathbf{x}}_{k-1}$. Furthermore, the system includes saturation checks: if the signal amplitude of any anchor exceeds the linear range of the ADC (e.g., due to close proximity), that measurement is discarded from the cost function for the current iteration to prevent numerical bias. The complete runtime execution flow is detailed in Algorithm 2.

C. Sensor Fusion with Onboard State Estimation

The absolute position estimate provided by the magnetic localization pipeline is fused with the UAV's high-rate onboard sensors to obtain a robust state estimate for feedback control. We utilize the nano-UAV stock EKF, which runs onboard the MCU. Notably, the UWB localization is natively supported, with the fusion architecture depicted in Figure 3.

The position estimate $\hat{\mathbf{x}}_k$ output by the Nelder-Mead optimizer in Algorithm 2 is treated as an asynchronous absolute position measurement update for the EKF. The measurement noise covariance matrix \mathbf{R}_{mag} associated with these updates

Algorithm 1 Initial Static Calibration

Require: Reference pose \mathbf{x}_{ref} , Anchor poses $\{\mathbf{p}_i\}$, Number of samples N_{cal}
Ensure: Calibration coefficients $\mathcal{C} = \{C_1, \dots, C_4\}$

- 1: $\bar{\mathbf{v}}_{raw} \leftarrow \mathbf{0}$
- 2: **for** $k \leftarrow 1$ to N_{cal} **do** ▷ Data Accumulation
- 3: $\mathbf{v}_{raw} \leftarrow \text{EXTRACTSIGNALFEATURES}(\text{ADC_Buffer})$
- 4: $\bar{\mathbf{v}}_{raw} \leftarrow \bar{\mathbf{v}}_{raw} + \mathbf{v}_{raw}$
- 5: **end for**
- 6: $\bar{\mathbf{v}}_{raw} \leftarrow \bar{\mathbf{v}}_{raw}/N_{cal}$ ▷ Compute Mean Amplitude
- 7: **for** each anchor $i \in \{1 \dots 4\}$ **do**
- 8: $V_{model,i} \leftarrow \text{DIPOLEMODEL}(\mathbf{x}_{ref}, \mathbf{p}_i)$ ▷ Via Eq. 3
- 9: $C_i \leftarrow \bar{v}_{raw,i}/V_{model,i}$ ▷ Compute Gain
- 10: **end for**
- 11: **return** \mathcal{C}

Algorithm 2 Runtime MI Position Estimation Loop

Require: Raw_Signal \mathcal{S} , Calibration \mathcal{C} , Prev. EKF estimate $\hat{\mathbf{x}}_{k-1}$, Attitude $\hat{\mathbf{n}}_r$
Ensure: Current position estimate $\hat{\mathbf{x}}_k$

- 1: $\mathbf{v}_{raw} \leftarrow \text{SIGNALPROCESSING}(\mathcal{S})$
- 2: $\mathcal{S}_{active} \leftarrow \{1, \dots, 4\}$ ▷ Set of valid anchors
- 3: **for** each anchor i **do**
- 4: $V_{meas,i} \leftarrow v_{raw,i}/C_i$ ▷ Apply Calibration
- 5: **if** $V_{meas,i} > V_{sat_thresh}$ **then** ▷ Check Saturation
- 6: $\mathcal{S}_{active} \leftarrow \mathcal{S}_{active} \setminus \{i\}$ ▷ Exclude anchor
- 7: **end if**
- 8: **end for**
- 9: Define cost function (Eq. (4)) based on active anchors:
- 10: $J(\mathbf{x}) = \sum_{i \in \mathcal{S}_{active}} (V_{model,i}(\mathbf{x}, \hat{\mathbf{n}}_r) - V_{meas,i})^2$
- 11: $\mathbf{x}_{opt} \leftarrow \text{NELDERMEAD}(J, \text{start} = \hat{\mathbf{x}}_{k-1})$
- 12: **if** $\|\mathbf{x}_{opt} - \hat{\mathbf{x}}_{k-1}\| < \Delta_{outlier}$ **then** ▷ Outlier Rejection
- 13: $\hat{\mathbf{x}}_k \leftarrow \mathbf{x}_{opt}$
- 14: SEND TO EKF($\hat{\mathbf{x}}_k$)
- 15: **else**
- 16: continue
- 17: **end if**
- 18: **return** $\hat{\mathbf{x}}_k$

is tuned based on the static characterization of the system; specifically, the standard deviation parameters are set according to the values determined in [22], [57]. This direct injection of position allows the EKF to correct the drift inherent in the inertial integration and optical flow, effectively pinning the drone's frame of reference to the UGV frame $\{\mathcal{B}\}$.

While the magnetic system provides a 3D position estimate, the vertical component (z) is often the least observable axis in planar anchor configurations and can be noisy. To ensure robust altitude hold, we augment the system with a downward-facing Time-of-Flight (ToF) laser rangefinder (the VL53L1x series for STMicroelectronics). However, the integration of the ToF sensor presents a specific challenge in our heterogeneous setup: the UAV takes off from the back of the UGV, and as the drone performs a lateral maneuver to exit the UGV's footprint, the ground reference for the ToF sensor changes abruptly from the UGV's back to the floor, causing a discontinuity (step)

in the raw distance measurement. If fed directly to the EKF, this jump would be interpreted as a sudden gain in altitude, leading to destabilizing control reactions. To address this, we implemented a custom filtering logic (state machine) within the sensor driver. The algorithm monitors the numerical derivative of the raw distance measurement $\dot{d} \approx (d_k - d_{k-1})/\Delta t$. The logic operates as follows: (i) *Nominal Flight*: When the derivative is below a safety threshold ($\dot{d} < \delta_{thresh}$), the sensor is assumed to be tracking a continuous surface. The measurement is passed to the estimator with a standard compensation offset. (ii) *Discontinuity Detection* (The "Step"): When the drone flies off the UGV, a large spike in the derivative is detected ($\dot{d} > \delta_{thresh}$). The filter identifies this as a surface change rather than vertical motion. (iii) *Output Smoothing*: Upon detection of the step, the filter holds the previous valid compensated altitude value, effectively ignoring the jump in the raw data, while internally realigning the reference baseline d_{t_0} . This strategy allows the EKF to maintain a continuous estimate of the altitude relative to the takeoff frame, seamlessly transitioning from "relative-to-robot" to "relative-to-ground" measurements without requiring external triggers.

IV. SYSTEM ARCHITECTURE

In this work, we investigate heterogeneous cooperation and teaming of two markedly different robotic platforms—a legged robot and a nano-UAV. These robots differ substantially in onboard computation, payload capacity, sensing power budget, and physical size, which severely constrains the class of localization sensors that each platform can support. Moreover, to achieve practical and robust cooperation in real environments, the system must remain independent of any external infrastructure for localization, environmental sensing, and computation. The system described in this section has been designed explicitly around these requirements. For the scope of this paper, we selected two commercial platforms extendable with custom hardware and software.

The ground platform consists of a Unitree A1 quadrupedal robot equipped with a custom lightweight backpack for on-board sensing and computation. The robot has a nominal footprint of approximately $500 \text{ mm} \times 300 \text{ mm} \times 400 \text{ mm}$ and a mass of 12.0 kg in its base configuration, a battery of 91 Wh^{-1} , and is equipped with twelve torque-controlled joints and onboard proprioceptive sensing in the form of joint encoders and a 9-DoF IMU. The A1 supports payloads of up to 5 kg , of which 3.15 kg are used by the backpack, including an additional 96 Wh battery and an Intel NUC used for navigation and high-level processing. The backpack also serves as a rigid mounting structure for the localization hardware and the landing deck introduced in fig. 2 and detailed below.

The Crazyflie 2.1 is a palm-sized ($9.2 \text{ cm} \times 9.2 \text{ cm}$), open-source nano-quadrotor platform designed for research and education in aerial robotics. It features a modular architecture with expansion decks that enable rapid prototyping of sensors, actuators, and communication systems. The onboard STM32F4 microcontroller handles flight control and sensor fusion. Equipped with a 9-DoF IMU, we extended its onboard

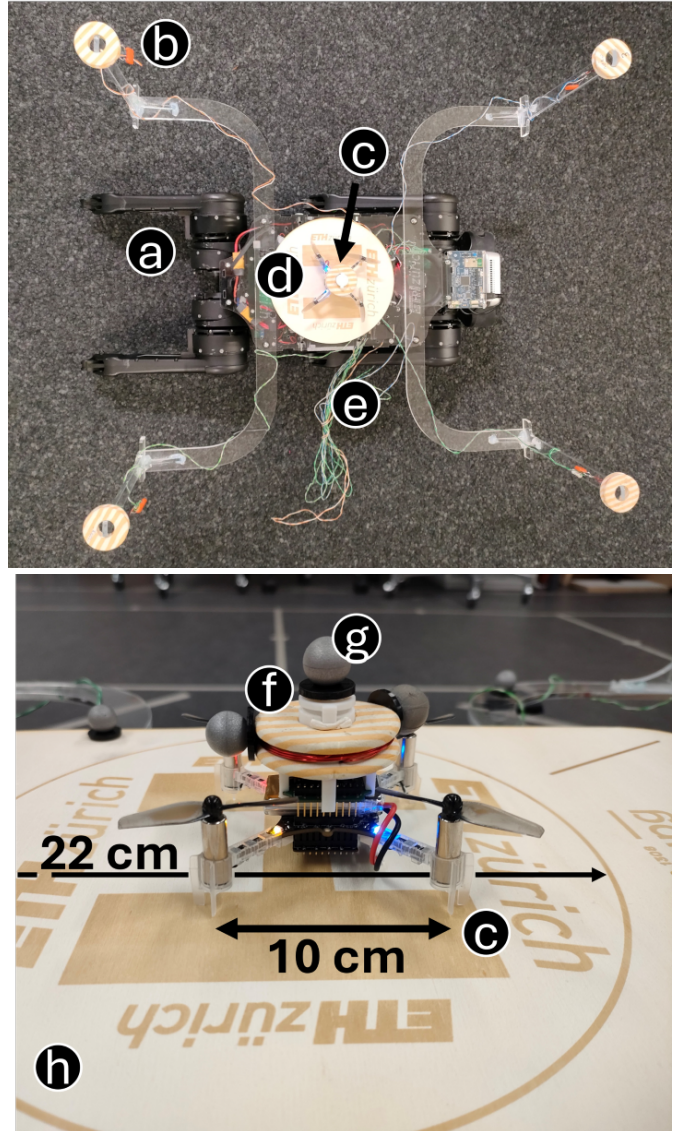


Fig. 2: Custom Magnetic Hardware. (a) The Unitree AI legged robot UGV. (b) One of the four lightweight MI coils used for precise localization. (c) The Crazyflie 2.1 nano-UAV. (d) The landing pad with a diameter of 22 cm mounted on UGV. (e) The wiring for the AnchorDeck and the four coils, plus the connections for the wireless battery charger. (f) The ultra-lightweight MI coil mounted on the Crazyflie 2.1 nano-UAV and the MagneticDeck. (g) Motion capture system markers used to assess the system performances.

sensors with the *Flow deck v2* from Bitcraze. The total power budget available for sensing and computation is $\sim 1 \text{ W}$ [8]. We selected the Crazyflie 2.1 because it offers a unique combination of low weight, extensibility, and real-time control, making it ideal for experiments where SWaP constraints are critical.

Figure 2 outlines the overall system architecture. The UGV is equipped with a landing pad with a size of $25 \text{ cm} \times 44 \text{ cm}$ made with transparent plexiglas (PMMA) and Polywood. The Crazyflie recharging coil (based on the *Qi 1.2 charger deck* from Bitcraze) is positioned in the marked area, with a $\varnothing 22 \text{ cm}$, which the UAV has to center during landing. Therefore, to center the nano-UAV inside the landing area,

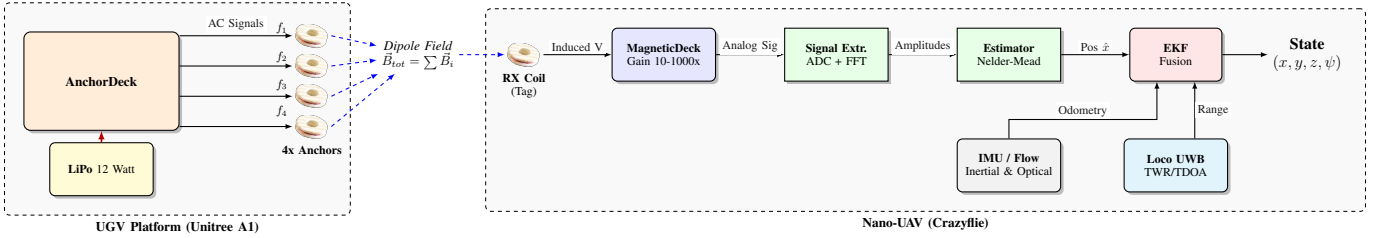


Fig. 3: System Overview Block Diagram. The *AnchorDeck* (orange box) houses the signal generation and driving logic, powered by the UGV battery. It directly drives four independent anchor coils. The magnetic field is received by the UAV, processed alongside UWB and IMU data within the EKF for state estimation.

the relative landing precision needs to provide a consistent accuracy < 10 cm. Four transmitting coils are mounted on rigid supports attached to the quadruped’s backpack (Figure 2), positioned at each corner with a $\varnothing 2$ cm plexiglas pipe 25 cm tall. On the other side, a single receiving coil is mounted on the Crazyflie using a custom 3D-printed holder. These constitute the key hardware elements of the magnetic anchor-tag system: the four coils on the legged robot act as anchors, and the receiving coil on the UAV acts as the tag. The coils, shown in detail in Figure 2, were hand-wound around lightweight, non-ferromagnetic supports. The total weight of the Crazyflie is 47 g, of which 9 g are added by the coil and the holder. The receiving coil mounted on the Crazyflie connects to a dedicated conditioning board, the *MagneticDeck* (Figure 2). The deck provides solder pads for the coil terminals and includes a parallel capacitor to establish an initial resonant gain. Beyond resonance, the *MagneticDeck* includes two amplification stages: (i) a fixed-gain $10\times$ amplifier, and (ii) a digitally programmable amplifier up to $100\times$ dynamically controlled by the onboard MCU. The final stage of the amplification and conditioning system is connected to the MCU internal 12-bit ADC, sampling at 518 kHz. The received voltage is a modulation of the four anchor signals; the amplitude and main frequency components of each must be extracted in the frequency domain, as described in Section IV-A.

All coils share identical parameters—the number of turns, wire type, and diameter—except for unavoidable manufacturing tolerances, ensuring consistent magnetic behavior. Specifically, each coil has a radius of 1.9 cm and 5 turns. Each anchor coil on the quadruped generates an AC magnetic dipole field by driving a sinusoidal current at a unique frequency (210, 199, 189, and 181 kHz). Conversely, the tag coil on the UAV behaves as a passive sensor: immersed in the superposition of the four dipole fields, it generates an electromotive force proportional to the received magnetic flux.

Two independent body frames and coordinate are present throughout the system, which need to be aligned: one relative to the quadruped’s body (and moving with it), and one attached to the UAV. The Crazyflie initializes its own frame at startup using onboard inertial sensors; due to drift, the magnetic localization system subsequently provides the primary absolute reference, effectively tying the UAV frame to the quadruped frame.

A. Magnetic Deck on the nano-UAV

Figure 3 shows the full processing chain. After amplification, the signal is digitized by the Crazyflie’s onboard ADC. A Flattop window is applied to increase amplitude accuracy, and a real-time FFT isolates the four frequency components, each corresponding to a different anchor. Peak amplitude estimates are refined via standard parabolic interpolation around the FFT bin associated with the anchor’s excitation frequency. For anchor k , the sinusoid at frequency f_k appears at FFT bin b_k with interpolated amplitude A_k . These amplitudes are forwarded to the magnetic inverse-dipole localization module. The estimated position is then fused in the Crazyflie’s EKF along with inertial, UWB, and optical-flow data.

V. EXPERIMENTAL EVALUATION

Experiments were conducted in an indoor flight arena equipped with a multi-camera motion capture system (Vicon), utilized *exclusively* to provide ground truth (GT) for validation. We employed the heterogeneous system architecture detailed in Section IV.

The system evaluation, which includes RMSE and landing success rate, relies on the coordinate frames $\{B\}$ (Anchor/UGV Body) and $\{U\}$ (Tag/UAV Body) defined in Section III. For this reason, motion capture markers were placed on both robots to track their poses in the world frame $\{W\}$, as visible in Figure 2. For quantitative assessment, all quantities (including motion-capture GT and the nano-UAV onboard EKF estimate driven by the magnetic localization) are expressed in the world frame $\{W\}$ by applying the corresponding rigid-body transforms (e.g., ${}^W T_B$) at each timestep.

A. Field Experimental Protocol

The experimental protocol is depicted in Figure 4 and defined as follows: upon the first system startup, the initial static calibration Algorithm 1 is executed to normalize per-anchor gains. It requires few seconds during which the overall system is static. After calibration, the nano-UAV autonomously takes off and executes the mission; for subsequent missions following a landing, the calibration is not repeated and the previously estimated gains are used. For the scope of this paper, we evaluate the MI localization system versus the landing supported by onboard sensors, e.g., IMU and optical flow. Evaluation of the UWB approach and landing is not performed, since the precision of this protocol is well

studied in the literature [14], [15] and its typical accuracy (10 cm to 30 cm) is better suited to long-range acquisition than to the final docking phase. However, we consider UWB localization as a valid solution for long range missions (UAV-UGV distance >1 m).

We evaluate the system across three scenarios and a comparative baseline: (i) **Baseline** (Flow-only): the nano-UAV holds position and track the UGV using only its native sensing stack (IMU + optical flow), with magnetic aiding disabled. This serves as a baseline to benchmark the drift accumulation inherent to infrastructure-less nano-UAVs in comparison with our MI positioning. (ii) **S1** (Static Hovering & Landing): the UGV remains stationary. The nano-UAV stabilizes at a setpoint \mathbf{x}_{ref} above the docking pad using magnetic localization, then performs an autonomous precision landing. This test aims to measure the drift accumulation and positioning noise over time. The movement sequence is shown in Figure 4a, Figure 4b, Figure 4c. (iii) **S2** (Linear Tracking & Landing): the UGV executes bounded planar motions (forward–backward). The nano-UAV tracks the moving reference frame $\{B\}$ and attempts autonomous landing while the landing pad is in motion. The movement sequence is shown in Figure 4d. (iv) **S3** (Composite Motion Tracking): this tests simulate a UGV-UAV shared mission, where the nano-UAV works as flying sensor for the ground legged robot. The UGV follows complex piecewise-smooth trajectories involving changes in speed and direction, while the nano-UAV is commanded to maintain a fixed relative hover position. The movement sequence is shown in Figure 4g.

B. Evaluation Metrics

The system performance for relative tracking and landing accuracy are evaluate through the position RMSE and the success rate. To quantify tracking accuracy, we compute the 3D RMSE in Equation (5) between the UAV position and the GT over N samples, where $\mathbf{p}_B^{\text{est}}$ is the onboard position estimate and \mathbf{p}_B^{GT} is the ground truth. We also report axis-wise RMSE (x, y, z) to analyze anisotropy.

$$\text{RMSE}_{3D} = \sqrt{\frac{1}{N} \sum_{k=1}^N \|\mathbf{p}_B^{\text{est}}(k) - \mathbf{p}_B^{\text{GT}}(k)\|^2}. \quad (5)$$

Regarding the success rate, a trial is considered successful if the UAV completes the task (hovering or landing or both) without strictly violating safety bounds. We declare *failure* if: (i) the instantaneous position error exceeds 0.5 m (safe volume violation), or (ii) the controller aborts due to signal loss or estimator divergence.

VI. EXPERIMENTAL RESULTS

We validate the proposed infrastructure-less MI localization system through extensive real-world experiments. The evaluation focuses on three key aspects: (i) quantitative tracking accuracy in static and dynamic docking scenarios, (ii) qualitative robustness compared to a standard onboard vision-based baseline, and (iii) feasibility within the strict constraints of

TABLE II: Scenario S1: The UGV is static. For Hovering, the UAV performs the sequence in Figure 4a, Figure 4b, Figure 4c. For the test *in-out*, the sequence includes also a movement (0.6 m) outside the landing pad. In summary, the sequence is: takeoff, fly 0.6 m ahead, fly back, landing. Values represent RMSE in centimeter, success rate (SC) in percentage.

Test	Hovering		in-out	
	Mag+Flow	Flow	Mag+Flow	Flow
1	1.14	4.56	6.93	FAIL
2	0.80	4.55	6.21	FAIL
3	1.79	2.56	FAIL	FAIL
4	1.76	5.36	6.94	FAIL
5	4.01	5.46	6.07	FAIL
6	7.11	3.24	15.7	—
7	8.11	1.28	6.03	—
8	2.84	2.58	6.01	—
9	11.6	6.93	5.40	—
10	11.5	0.65	5.79	—
Mean	5.01	3.72	7.23	N/A
SC	100%	100%	90%	0%

nano-scale aerial platforms.. All experiments compare the proposed method (Mag+Flow) against a baseline (Flow) that relies exclusively on the drone’s native optical flow and internal state estimator.

A. Static Hovering and Landing (S1)

In the first scenario (S1), the UGV acts as a stationary docking pad. The aerial agent performs a takeoff, stabilizes at a reference altitude of 45 cm, and executes an autonomous landing. Quantitative results, summarized in Table II, demonstrate that the magnetic aiding effectively eliminates the position drift inherent in dead-reckoning solutions.

The proposed system achieves a 3D RMSE below 10 cm for the Hovering sequence, with an aggregate mean of approximately 5 cm. This precision ensures that the UAV remains reliably centered over the $\varnothing 22$ cm landing pad. Only in Test 9-10, the landing position is not perfectly centered on the landing pad, but not considered as *failure*. Figure 5 visually illustrates the touchdown accuracy achieved by the proposed Mag+Flow method, with landing points tightly concentrated around the setpoint. For completeness, Table II reports the corresponding quantitative results, including the Optical-Flow-only baseline for comparison. Any slight differences in favor of the Flow deck are likely within the variability of the touchdown transient (e.g., small oscillations during contact and ground effect induced disturbances) rather than reflecting a systematic advantage of the sensing modality.

This aspect is evident in a slightly different experiment, in fact, in addition to the nominal hover-and-land trials, we performed an extra out-and-back lateral offset maneuver (reported as *in-out* in Table II): with the UGV still stationary, the UAV takes off, translates along the x direction to a setpoint displaced by 0.6 m from the docking-frame origin, and then returns toward the pad. This additional test stresses drift accumulation away from the docking region before the landing phase. In these *in-out* trials, the Flow-only baseline repeatedly violates the safety geofence (>0.5 m error) before a landing

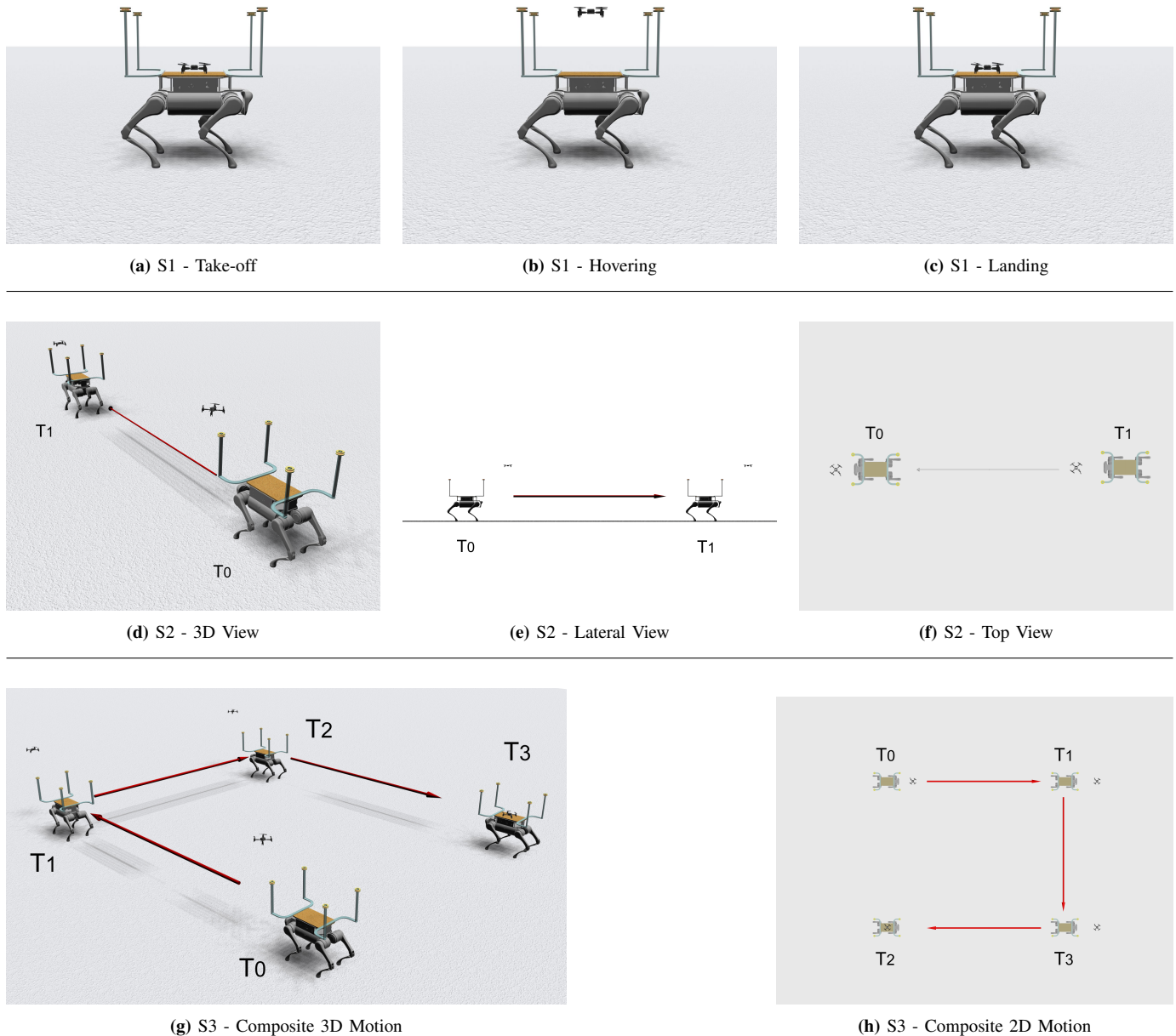


Fig. 4: Visual overview of the experimental validation scenarios using the proposed magnetic localization system. **(a)-(c) S1 (Static Hovering & Landing):** The nano-UAV performs an autonomous sequence of takeoff, hovering, and precision landing on the stationary UGV. **(d)-(f) S2 (Linear Tracking & Landing):** The nano-UAV tracks the UGV moving along a linear trajectory. Visualization includes (d) 3D perspective, (e) lateral view showing the relative distance maintenance (T_0 to T_1), and (f) top-down view of the alignment. **(g)-(h) S3 (Composite Motion Tracking):** The UAV tracks and follows the UGV performing complex planar maneuvers with varying velocity and direction, maintaining the relative position within the magnetic workspace.

can be attempted, whereas Mag+Flow remains bounded and enables the subsequent precision landing keeping the 3D RMSE below 10 cm.

B. Dynamic Tracking and Docking (S2 & S3)

The system's capabilities were further stressed in dynamic scenarios where the UGV executes linear back-and-forth motions (S2) and complex composite planar trajectories (S3).

Quantitative results, summarized in Table III, confirm that the onboard estimator tracks the moving reference frame

TABLE III: Linear tracking and composite motion results. Performance comparison during UGV planar forward-backward motion (S2) and during complex UGV trajectories (S3). RMSE calculated on the whole path. Values represent RMSE in centimeter, success rate (SC) in percentage.

	1	2	3	4	5	6	7	8	9	10	Mean	SC
S2	6.04	14.7	7.11	6.09	10.7	5.56	13.5	FAIL	6.51	FAIL	8.77	80%
S3	9.39	8.14	27.1	7.14	11.3	7.09	7.34	8.52	9.53	9.46	10.5	100%

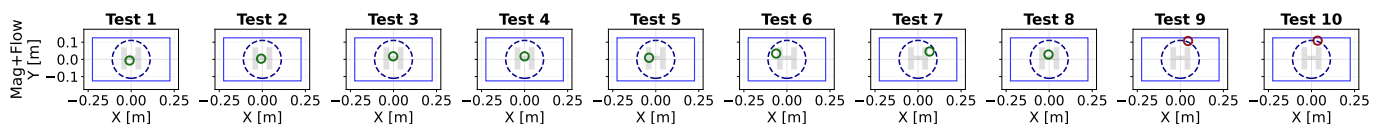


Fig. 5: Touchdown accuracy analysis for scenario **S1-Hovering**. The plot shows the planar 2D position of the UAV relative to the docking pad center at the moment of landing for the proposed Mag+Flow method (circles).

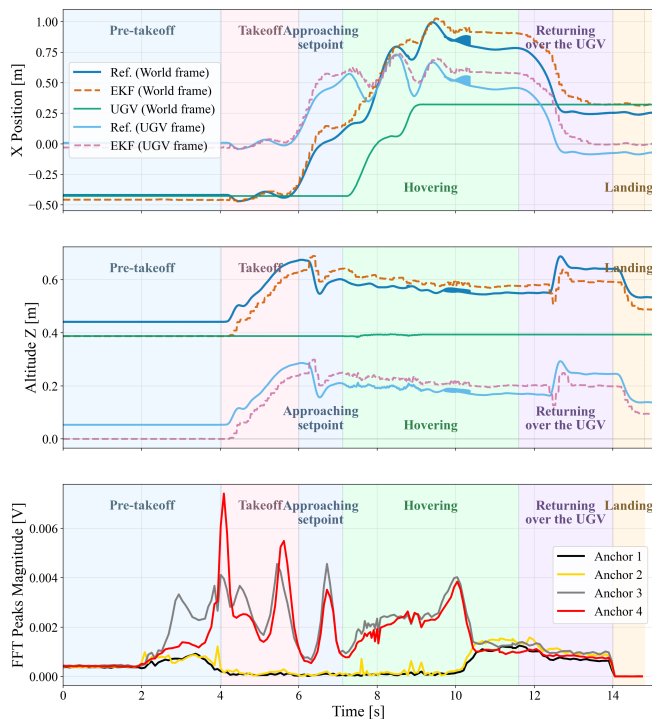


Fig. 6: Scenario **S2**: time-history qualitative results for a representative linear docking sequence. The colored bands highlight the mission phases (pre-takeoff, takeoff/approach, hovering, return over the UGV, landing). Top: x position in the world frame. Middle: altitude z . Bottom: magnitude of the FFT peaks of the coil voltage, which provides a proxy of the received magnetic signal strength over time.

with an average 3D RMSE in the range of 8cm to 11cm and a success rate between 80% and 100%, defining system accuracy and robustness, respectively. A representative trial for Scenario **S3** is shown in Figure 7, where the estimated trajectory is compared against the UGV reference in the world frame. Therefore, Table III does not represent the landing accuracy, as reported in Table II, but instead the RMSE on the whole trajectory (including landing) referred to the expected trajectory. Figure 6 and Figure 7 depict an example of the movement sequence used to calculate the RMSE in Table III.

Figure 6 provides a detailed breakdown of the system’s behavior during the linear docking sequence (S2) using the magnetic localization. The shaded bands segment the mission into intuitive phases (pre-takeoff, approach, hovering, return, and landing) and allow directly relating the estimator outputs to the flight state. The first two plots report the UAV position along the x axis and the altitude z over time, highlighting

the approach to the setpoint and the subsequent return over the UGV. The third plot shows the power spectrum magnitude extracted from the receiving-coil voltage: as the relative geometry changes during the maneuver, the received signal strength varies accordingly, providing an intuitive proxy of link quality throughout the sequence.

From this visual analysis, two key characteristics emerge. First, the ‘before takeoff’ pose often exhibits a slight static offset below 5 cm on the xy plane, highlighting minor residual imperfections in the initial magnetic calibration, a behavior that does not significantly affect the system robustness and performance. Second, while the planar trajectories show high repeatability and consistent tracking, oscillations are observable during the transient phases of takeoff and landing (Figure 6-Approaching setpoint & Hovering). These fluctuations are primarily attributed to the tuning of the flight controller rather than to instability in the magnetic localization estimate.

For Scenario **S3**, Figure 7 complements the quantitative metrics with a time-aligned qualitative view: numbered video snapshots (markers 1–7) are synchronized with the corresponding dashed vertical markers in the logged signals, enabling a phase-by-phase interpretation of the maneuver. In the 3D plot, the *Ref. (World frame)* trajectory is shown in blue, the *UGV (World frame)* trajectory in green, and the *EKF (World frame)* estimate as an orange dashed line. Similar to S2, small oscillations are visible during the initial takeoff/settling (markers 1–2), while the tracking error remains bounded for most of the trial. Noticeable error increases occur mainly at trajectory transitions and, more critically, around marker 6 (approximately at $t \approx 13$ s), where the UAV crosses the UGV footprint and the downward ToF ground reference changes abruptly from the deck to the floor. As discussed in Sec. III-C, we mitigate this effect with a dedicated step-detection and smoothing logic in the ToF driver; nevertheless, the residual discontinuity can still be perceived by the controller as an abrupt vertical variation, temporarily exciting oscillations and producing a corresponding increase in the tracking error (consistent with the snapshot associated to marker 6).

C. System Integration

The experimental campaign validated the initial and final stage of docking, focusing on the MI localization performances, this paper scope. However, integration with UWB is trivial and well documented in previous works, such as [8], [14]. With the combination of the two solutions, already supported by the EKF used in the Crazyflie, the nano-UAV mission range is increased up to the physical limitations of UWB connectivity, which could reach >100 m. The maximum

measured working range of the MI system is ~ 1 m (depending on environmental conditions), which perfectly pairs with the 10 cm to 30 cm UWB accuracy for the initial/final docking phases.

D. Limitations

While the system performs robustly during translational maneuvers, a limitation was identified regarding UGV Yaw rotation maneuvers. The current magnetic model assumes a fixed orientation of the anchor dipoles or purely translational relative motion. Consequently, rapid yaw rotations of the UGV introduce unmodeled variations in the magnetic field map, which the position-only solver may misinterpret as translational displacement. This currently restricts the operational envelope to planar translations with limited heading changes ($\pm 20^\circ$), suggesting that future iterations should incorporate full 6-DoF magnetic pose estimation to decouple relative rotation from translation. However, upgrading the estimator to a full 6-DoF pose solver (solving for $SE(3)$) would decouple the relative orientation from the position, albeit at a higher computational cost.

In practice, this limitation only restricts the UGV turn paths to 20° around a single point, not impairing complex maneuvers. Indeed, for bigger rotation angles, the UGV just need to walk forward during the rotation avoiding the solver misinterpretation. The main unsupported movement is a 180° rotation to invert direction around the same point.

VII. DISCUSSION

The experimental validation confirms that near-field magneto-inductive localization can serve as a robust, infrastructure-less navigation bridge for nano-UAVs operating in close proximity to a mobile ground base. A key advantage highlighted by the comparison with the baseline (Section VI) is the immunity of the magnetic system to visual aliasing. In dynamic docking scenarios, standard infrastructure-less state estimators fails because the local frame aligns with the static global frame rather than the moving platform, leading to uncontrolled drift. Conversely, the proposed MI system locks the UAV's position relative to the field generated by the UGV anchors. This physical link ensures that the relative position estimate remains consistent regardless of the surrounding texture, lighting conditions, or the global motion of the ground robot. In contrast to permanent-magnet docking approaches, where magnetics mainly provide passive short-range capture, our frequency-division MI beacons define a structured measurement model for relative navigation: anchor contributions are separable in the frequency domain, enabling unambiguous data association and online link-quality monitoring while attenuating DC/low-frequency disturbances. In line with this, Figure 6 qualitatively shows how the received magnetic signal evolves across the flight phases, providing a direct indication of link quality during the maneuver. This feature is critical for operations in unstructured environments (e.g., caves or disaster sites) where GNSS and external illumination are unavailable.

The system architecture was designed to handle the extreme asymmetry between the two robotic platforms. By shifting the

power-hungry components (transmitting coils and drivers) to the quadruped—which has orders of magnitude more battery capacity—and keeping the UAV side passive and lightweight, we respect the strict SWaP constraints of the nano-UAV. The receiving hardware adds less than 9 g to the UAV's mass, and the full onboard workflow (Figure 3) runs at 20 Hz in real time without impacting the other nano-UAV MCU tasks. This efficiency implies that the solution is scalable to even smaller platforms or swarms, provided that the UGV can host the emitters.

VIII. CONCLUSION AND FUTURE WORK

This paper presented the design and validation of a fully onboard, infrastructure-less MI localization system enabling heterogeneous interaction between a nano-UAV and a quadrupedal robot. By leveraging frequency-multiplexed magnetic beacons, we demonstrated that a 47 g drone can autonomously hover, track, and land on a moving platform with centimeter-level precision, independent of GNSS or external motion capture systems.

The experimental results show that the system achieves a positioning RMSE of approximately 5 cm in static hovering and maintains an accuracy between 8 cm to 11 cm while tracking a moving UGV. In all field experiments, the success rate is always above 80%. This performance significantly outperforms standard methods, listed in Table I, which consistently fail in dynamic docking scenarios due to the lack of an absolute relative reference. Furthermore, the optimized implementation proves that complex nonlinear magnetic inversion is feasible in real-time (20 Hz) on resource-constrained robotic platforms.

This paper poses foundations for advancing the heterogeneous robotic cooperation in complex scenarios, proposing a solid system validated in the field with an UGV and a nano-UAV.

SUPPLEMENTARY MATERIAL

Supplementary video at <https://www.youtube.com/watch?v=rqQ7IGnRazo>

Project's code at <https://provided-after-review>

REFERENCES

- [1] B. Zhou *et al.*, "Racer: Rapid collaborative exploration with a decentralized multi-uav system," *IEEE Transactions on Robotics*, vol. 39, no. 3, pp. 1816–1835, 2023.
- [2] L. Lanča *et al.*, "Probabilistic modeling and control for multi-uav search over uneven terrain," *IEEE Transactions on Robotics*, vol. 42, pp. 418–438, 2025.
- [3] H. Xu *et al.*, "Omni-swarm: A decentralized omnidirectional visual-inertial-uwB state estimation system for aerial swarms," *Ieee transactions on robotics*, vol. 38, no. 6, pp. 3374–3394, 2022.
- [4] S. Javed *et al.*, "State-of-the-art and future research challenges in uav swarms," *IEEE Internet of Things Journal*, vol. 11, no. 11, pp. 19 023–19 045, 2024.
- [5] X. Cai *et al.*, "Energy-aware, collision-free information gathering for heterogeneous robot teams," *IEEE Transactions on Robotics*, vol. 39, no. 4, pp. 2585–2602, 2023.
- [6] M. Tranzatto *et al.*, "CERBERUS in the darpa subterranean challenge," *Science Robotics*, vol. 7, no. 66, 2022.
- [7] S. Zhang *et al.*, "Heterogeneous targets trapping with swarm robots by using adaptive density-based interaction," *IEEE Transactions on Robotics*, vol. 40, pp. 2729–2748, 2024.

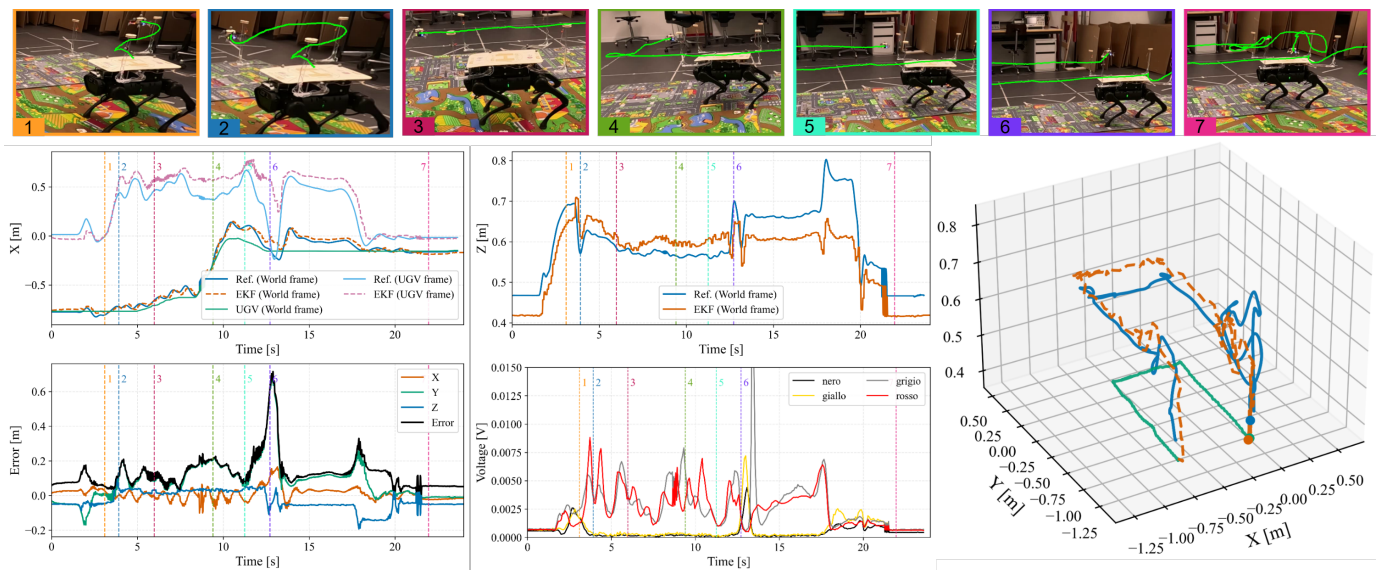


Fig. 7: Scenario S3 (Test 1): qualitative time-aligned analysis of dynamic tracking. The numbered markers (1–7) identify key flight phases via synchronized video snapshots and the corresponding dashed vertical lines in the time traces. The trajectory plots (3D and top-down) compare *Ref.* (World frame), *UGV* (World frame), and *EKF* (World frame). Markers 1–2 (early takeoff/settling) highlight small transient oscillations.

- [8] V. Niculescu *et al.*, “Ultra-lightweight collaborative slam for robot swarms,” *IEEE Access*, 2025.
- [9] L. Yang *et al.*, “A survey on swarm microrobotics,” *IEEE Transactions on Robotics*, vol. 38, no. 3, pp. 1531–1551, 2021.
- [10] R. G. Ribeiro *et al.*, “Unmanned-aerial-vehicle routing problem with mobile charging stations for assisting search and rescue missions in postdisaster scenarios,” *IEEE transactions on systems, man, and cybernetics: Systems*, vol. 52, no. 11, pp. 6682–6696, 2021.
- [11] M. Pourjabar *et al.*, “Land & localize: An infrastructure-free and scalable nano-drones swarm with uwb-based localization,” in *2023 19th International Conference on Distributed Computing in Smart Systems and the Internet of Things (DCOSS-IoT)*. IEEE, 2023, pp. 654–660.
- [12] S. A. Chien *et al.*, “Exploring beyond earth using space robotics,” *Science Robotics*, vol. 9, no. 91, p. eadi6424, 2024.
- [13] X. Zhou *et al.*, “Swarm of micro flying robots in the wild,” *Science Robotics*, vol. 7, no. 66, p. eabm5954, 2022.
- [14] D. Schindler *et al.*, “A relative infrastructure-less localization algorithm for decentralized and autonomous swarm formation,” in *2023 IEEE/RSJ International Conference on Intelligent Robots and Systems (IROS)*. IEEE, 2023, pp. 5288–5295.
- [15] T. Polonelli *et al.*, “Performance comparison between decawave dw1000 and dw3000 in low-power double side ranging applications,” in *2022 IEEE Sensors Applications Symposium (SAS)*. IEEE, 2022, pp. 1–6.
- [16] D. Mikhaylov *et al.*, “Toward the future generation of railway localization exploiting rtk and gnss,” *IEEE Transactions on Instrumentation and Measurement*, vol. 72, pp. 1–10, 2023.
- [17] J. Liu *et al.*, “An integrated uwb-vision framework for autonomous approach and landing of uavs in gps-denied environments,” *Mathematical Foundations of Computing*, vol. 8, pp. 710–724, 1 2025.
- [18] J. Lin *et al.*, “Low-complexity control for vision-based landing of quadrotor uav on unknown moving platform,” *IEEE Transactions on Industrial Informatics*, vol. 18, no. 8, pp. 5348–5358, 2021.
- [19] G. Niu *et al.*, “Vision-based autonomous landing for unmanned aerial and ground vehicles cooperative systems,” *IEEE robotics and automation letters*, vol. 7, no. 3, pp. 6234–6241, 2021.
- [20] P. Ladosz *et al.*, “Autonomous landing on a moving platform using vision-based deep reinforcement learning,” *IEEE Robotics and Automation Letters*, vol. 9, no. 5, pp. 4575–4582, 2024.
- [21] H. A. Foudeh *et al.*, “An advanced unmanned aerial vehicle (uav) approach via learning-based control for overhead power line monitoring: A comprehensive review,” *IEEE Access*, vol. 9, pp. 130410–130433, 2021.
- [22] V. Brunacci *et al.*, “Fusion of uwb and magnetic ranging systems for robust positioning,” *IEEE Transactions on Instrumentation and Measurement*, vol. 73, pp. 1–12, 2023.
- [23] P. K. Chittoor *et al.*, “Wireless-sensor communication based wireless-charging coil positioning system for uavs with maximum power point tracking,” *IEEE Sensors Journal*, vol. 22, no. 8, pp. 8175–8182, 2022.
- [24] L. Zheng *et al.*, “Aage: Air-assisted ground robotic autonomous exploration in large-scale unknown environments,” *IEEE Transactions on Robotics*, 2025.
- [25] T. Miki *et al.*, “Learning robust perceptive locomotion for quadrupedal robots in the wild,” *Science robotics*, vol. 7, no. 62, p. eabk2822, 2022.
- [26] A. Lin *et al.*, “One filter to deploy them all: Robust safety for quadrupedal navigation in unknown environments,” *IEEE Transactions on Robotics*, vol. 42, pp. 545–560, 2025.
- [27] D. Hoeller *et al.*, “Anymal parkour: Learning agile navigation for quadrupedal robots,” *Science Robotics*, vol. 9, no. 88, p. eadi7566, 2024.
- [28] A. Agarwal *et al.*, “Legged locomotion in challenging terrains using egocentric vision,” in *Conference on robot learning*. PMLR, 2023, pp. 403–415.
- [29] D. Kim *et al.*, “Vision aided dynamic exploration of unstructured terrain with a small-scale quadruped robot,” in *2020 IEEE International Conference on Robotics and Automation (ICRA)*. IEEE, 2020, pp. 2464–2470.
- [30] A. Ochoa-de-Eribe-Landaberea *et al.*, “Uwb and imu-based uav’s assistance system for landing operations in wind turbine inspection,” *Sensors*, vol. 22, no. 7, p. 2599, 2022.
- [31] S. Ha *et al.*, “Learning-based legged locomotion: State of the art and future perspectives,” *The International Journal of Robotics Research*, vol. 44, no. 8, pp. 1396–1427, 2025.
- [32] C. Liu *et al.*, “A review of collaborative air-ground robots research,” *Journal of Intelligent & Robotic Systems 2022 106:3*, vol. 106, pp. 60–103, 2022.
- [33] P. Tokekar *et al.*, “Sensor planning for a symbiotic UAV and UGV system for precision agriculture,” *IEEE Transactions on Robotics*, vol. 32, no. 6, pp. 1498–1511, Dec. 2016.
- [34] T. Polonelli *et al.*, “An open platform for efficient drone-to-sensor wireless ranging and data harvesting,” *Sustainable Computing: Informatics and Systems*, vol. 35, p. 100734, 2022.
- [35] Y. Yue *et al.*, “Tightly-coupled perception and navigation of heterogeneous land-air robots in complex scenarios,” in *2021 IEEE International Conference on Robotics and Automation (ICRA)*. IEEE, 2021, pp. 10052–10058.
- [36] B. A. Ferreira *et al.*, “Heterogeneous multirobot team: Maritime inspection and intervention in global navigation satellite system-denied scenarios,” *IEEE robotics & automation magazine*, 2025.
- [37] M. Krogius *et al.*, “Flexible layouts for fiducial tags,” in *2019 IEEE/RSJ International Conference on Intelligent Robots and Systems (IROS)*, 2019.

- [38] A. Salagame *et al.*, “Practical challenges in landing a uav on a dynamic target,” *arXiv preprint arXiv:2209.14465*, 2022.
- [39] X. Yu *et al.*, “A quadrotor aerial docking system utilizing both vision and magnetic field,” *IEEE Robotics and Automation Letters*, 2025.
- [40] N. P. Nguyen *et al.*, “Persistent charging system for crazyflie platform,” *Drones*, vol. 6, no. 8, p. 212, 2022.
- [41] A. E. De Silva *et al.*, “Uav-ugv collaborative localisation with minimum sensing,” *Sensors*, vol. 24, no. 14, p. 4629, 2024.
- [42] Y. Zhang *et al.*, “Air-ground collaborative robots for fire and rescue missions: Towards mapping and navigation perspective,” *arXiv preprint arXiv:2412.20699*, 2024.
- [43] T.-M. Nguyen *et al.*, “Viral-fusion: A visual-inertial-ranging-lidar sensor fusion approach,” *IEEE Transactions on Robotics*, vol. 38, no. 2, pp. 958–977, 2021.
- [44] Y. Feng *et al.*, “Autonomous landing of a uav on a moving platform using model predictive control,” *Drones*, vol. 2, no. 4, p. 34, 2018.
- [45] T. Bába *et al.*, “Autonomous landing on a moving vehicle with an unmanned aerial vehicle,” *Journal of Field Robotics*, vol. 36, no. 5, pp. 874–891, 2019.
- [46] L. Deng *et al.*, “Self-spin enabled docking and detaching of a uav-ugv system for aerial-terrestrial amphibious and independent locomotion,” *IEEE Robotics and Automation Letters*, vol. 8, no. 5, pp. 2454–2461, 2023.
- [47] M. N. Alghanim *et al.*, “Comparison of controller performance for ugv-landing platform self-leveling,” in *2020 28th Mediterranean conference on control and automation (MED)*. IEEE, 2020, pp. 471–478.
- [48] L. Lan *et al.*, “An induction-based localisation technique for wirelessly charged drones,” in *2020 IEEE PELS Workshop on Emerging Technologies: Wireless Power Transfer (WoW)*. IEEE, 2020, pp. 275–277.
- [49] P. Serra *et al.*, “Landing of a quadrotor on a moving target using dynamic image-based visual servo control,” *IEEE Transactions on Robotics*, vol. 32, no. 6, pp. 1524–1535, 2016.
- [50] B. Yuan *et al.*, “High speed safe autonomous landing marker tracking of fixed wing drone based on deep learning,” *IEEE Access*, vol. 10, pp. 80 415–80 436, 2022.
- [51] C. V. Nguyen *et al.*, “A novel framework of visual detection, tracking and landing for uavs utilizing ar markers,” in *2023 International Conference on Control, Robotics and Informatics (ICCRI)*. IEEE, 2023, pp. 81–85.
- [52] H. Khoirunnisa *et al.*, “Implementation of ir lock on poledrone (polman drone education) for precision landing with ros,” in *2023 IEEE 15th International Conference on Computational Intelligence and Communication Networks (CICN)*. IEEE, 2023, pp. 584–590.
- [53] D. Sun *et al.*, “Parallel robotic automated docking method for realizing space segment assembly,” *Scientific Reports*, vol. 15, no. 1, p. 5754, 2025.
- [54] T. E. Abrudan *et al.*, “Distortion rejecting magneto-inductive 3-d localization,” *IEEE Journal on Selected Areas in Communications*, vol. 33, no. 11, pp. 2380–2390, 2015.
- [55] A. Markham *et al.*, “Underground localization in 3-d using magneto-inductive tracking,” *IEEE Sensors Journal*, vol. 12, no. 6, pp. 1809–1818, 2012.
- [56] A. Chavda *et al.*, “A magnetic induction based underground localization system for miner safety,” in *2023 IEEE Sensors*, 2023, pp. 1–4.
- [57] G. D. Angelis *et al.*, “Comparison of measurement models for 3d magnetic localization and tracking,” *IEEE Transactions on Instrumentation and Measurement*, vol. 66, no. 10, pp. 2543–2555, 2017.
- [58] J. Wu *et al.*, “Wireless power and data transfer via a common inductive link using frequency division multiplexing,” *IEEE Transactions on Industrial Electronics*, vol. 62, no. 12, pp. 7810–7820, 2015.
- [59] A. Moschitta *et al.*, “Analysis of simultaneous 3d positioning and attitude estimation of a planar coil using inductive coupling,” in *2017 IEEE International Instrumentation and Measurement Technology Conference (I2MTC)*, 2017, pp. 1–6.
- [60] M. Janosek *et al.*, “Magnetic calibration system with interference compensation,” *IEEE Transactions on Magnetics*, vol. 55, no. 1, pp. 1–4, 2019.
- [61] T.-T. Nguyen *et al.*, “Landing uav on moving surface vehicle: Visual tracking and motion prediction of landing deck,” in *2024 IEEE/SICE International Symposium on System Integration (SII)*. IEEE, 2024, pp. 827–833.
- [62] K. van Oosterhout *et al.*, “An approximate electromagnetic model for optimizing wireless charging of biomedical implants,” *IEEE Transactions on Biomedical Engineering*, vol. 69, no. 6, pp. 1954–1963, 2022.
- [63] G. De Angelis *et al.*, “Comparison of measurement models for 3d magnetic localization and tracking,” *Sensors*, vol. 17, no. 11, 2017.